Journal of Rock Mechanics and Geotechnical Engineering 18 (2026) 3348–3364

Contents lists available at ScienceDirect

Journal of Rock Mechanics and Geotechnical Engineering

journal homepage: www.jrmge.cn

Full Length Article

Impact of blast design parameters on rock fragmentation in sub-level caving: A multivariate regression approach

Ahmadreza Khodayari [a,*], Chaoshui Xu [a], Peter Dare-Bryan [b], Peter Dowd [a], Veljko Lapcevic [c], Andrew Metcalfe [a]

[a] School of Chemical Engineering, Faculty of Mining Engineering, The University of Adelaide, Adelaide, South Australia, 5000, Australia
[b] Orica, Perth, Western Australia, 6007, Australia
[c] Division of Mining and Geotechnical Engineering, Luleå University of Technology, Luleå, 971 87, Sweden

ARTICLE INFO

Article history:
Received 20 January 2025
Received in revised form
30 July 2025
Accepted 30 July 2025
Available online 26 November 2025

Keywords:
Sublevel caving
Mechanistic blast model
Ernest Henry mine
Multivariate regression analysis
Particle size distribution

ABSTRACT

Sub-level caving (SLC) is a mass mining method suitable for large, steeply dipping orebodies. The particle size distribution (PSD) of blasted material affects material flow through the stope. Improving blast-induced fragmentation can enhance draw point extraction, increasing ore recovery, reducing dilution, and lowering costs in loading and crushing. Numerical simulations using the Mechanistic Blasting Model (MBM) explored these improvements. MBM simulates the explosive loading, rock fracturing, and dynamic explosive gas effects. It addresses uneven explosive distribution from fan-shaped blast holes and complex broken ground conditions. The simulations used Ernest Henry Mine (EHM) data to define the baseline blast design and rock mass and compared field and modelled fragmentation sizes for varying explosive densities and burden sizes. Then, MBM simulations incorporated different rock mass fracture densities, tensile strengths and in-situ stresses, and further blast design changes in the blasthole diameter and charge spacings. A total of 34 scenarios were modelled. Multivariate regression analysis identified key parameters, and new regression models for P20, P50, and P80 passing sizes were developed and validated against the EHM and MBM simulation data. Additional simulations confirmed that while regression predictive models were slightly less accurate, they provided efficient predictions with acceptable accuracy.

1. Introduction

The initial step in the extraction process in metalliferous mining involves the fragmentation of rock masses that contain ore. Typically, this is achieved using methods such as drilling and blasting. The fragmentation size distribution after blasting may have an impact on the efficiency of downstream processes such as hauling and crushing (Grant et al., 1995; Jimeno et al., 1995; Aler et al., 1996; Hamdi et al., 2001; Campbell and Thurley, 2017). Fig. 1 depicts the process of sub-level caving. In each sublevel, a series of fan-shaped rings of blastholes is drilled. Blasting is carried out ring-by-ring, moving from the hanging wall to the footwall in a retreating manner. The blasted rock fragments flow into the production drift at the draw point and are excavated until dilution of the ore by the cave waste material becomes excessive (Shekhar, 2020). Finer particles are more mobile and flow faster to the draw point, but they can produce sticky mud or slurry in damp circumstances. In addition, fines can also produce dust problems in the operational areas (Campbell and Thurley, 2017). Furthermore, small fragments can have an impact on the flow characteristics within the stope, producing narrow draw - preferential flow in the central section of the ring (Manzoor, 2023). On the other hand, large rock fragments or boulders can produce severe hang-ups blocking the flow of material to the draw point, negatively impacting productivity and producing a safety hazard (Campbell and Thurley, 2017). In practice, achieving the optimal rock fragmentation size distribution is challenging due to the intricate interplay of multiple factors associated with blasting parameters, rock properties and operational conditions.

* Corresponding author.
E-mail address: Ahmadreza.khodayari@adelaide.edu.au (A. Khodayari).

Peer review under responsibility of Institute of Rock and Soil Mechanics, Chinese Academy of Sciences.

https://doi.org/10.1016/j.jrmge.2025.07.038

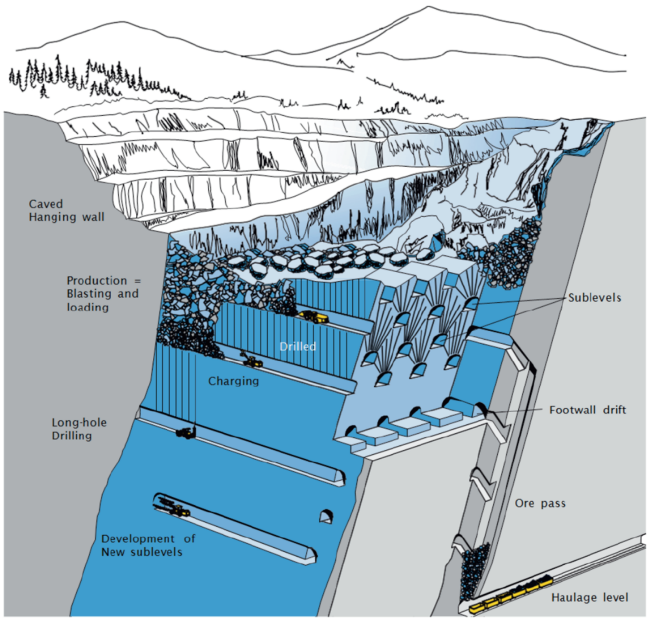

Fig. 1. Schematic layout of sublevel caving (Shekhar, 2020).

1.1. Empirical fragmentation models

Modelling rock fragmentation using blast design parameters and rock mass properties, remains a challenging topic for researchers and engineers (Onederra, 2004a). Several empirical models have been developed to evaluate the particle size distribution resulting from blasting. As discussed in Ouchterlony and Sanchidrián (2018), the simplest form of the cumulative distribution function was first developed as a power function by Gates, Gaudin and Schuhmann (GGS). GGS is based on the maximum sizes of rock fragments, normalising parameters and a shape (or slope) parameter (Ouchterlony and Sanchidrián, 2018). One of the most important cumulative distribution functions was developed by Rosin and Rammler. The original Rosin-Rammler (RR) size distribution function does not have any upper fragment size limit (Ouchterlony and Sanchidrián, 2018). The Weibull distribution later applied this function to a broader field of statistics and material strength, but it did not include an upper limit. The upper size limit was introduced by Sanchidrián et al. (2014) in response to the limitations of the original Weibull distribution (Weibull, 1951). Many empirical models developed after the RR distribution function were defined with their own parameters of median fragmentation size and uniformity index to improve accuracy. The models aimed to introduce a more complete description of the blast design and rock mass to increase the applicability of the model to different blasting scenarios. These models include the Kuz-Ram model (Koshelev et al., 1971; Cunningham, 1983, 1987), the extended Kuz-Ram model (Cunningham, 2005), the Swedish Detonic Research Foundation (SveDeFo) function (Hjelmberg, 1983; Ouchterlony and Sanchidrián, 2018), and the US Bureau of Mines (USBM) model (Stagg et al., 1990; Chung and Katsabanis, 2000). The original Kuz-Ram model took Koshelev and Kuznetsov's derived formula for the resulting average fragment size due to a quantity of high explosive and converted it to apply to commercial bulk explosives and a blast design powder factor, and the RR uniformity index was derived from blast design data (Koshelev et al., 1971; Cunningham, 1983, 1987, 2005).

Other models have been developed to address the underestimation of the Kuz-Ram model for fine fragments in blasted material (Djordjevic, 1998). These include the Crushed Zone Model and the Two-Component Model, both developed at the Julius Kruttschnitt Mineral Research Centre. Both models were built on the Kuz-Ram framework and divide the blasted material into coarse and fine fractions. In these models, the coarse material is due to tensile fracturing within the in-situ discontinuities in the rock mass, and the fines are modelled considering the crushed zone radius and the volume of material crushed around the blast hole. Esen et al. (2003) developed a formula to define the radius of the crushed zone using a crushing zone index. Onederra et al. (2004) defined a breakage zone in the shape of a star around the blast hole and tested this model using six blasts with good results. Based on data from the Ridgeway SLC mine, Onederra (2004b, 2005) linked the peak particle velocity breakage threshold to a breakage uniformity index and used the Two-Component Model to derive a fragmentation PSD curve and validate it against field data (Djordjevic, 1999; Esen et al., 2003; Onederra, 2004b; Onederra et al., 2004; Oñederra, 2005; Ouchterlony and Sanchidrián, 2018).

The FRAGMENTO framework was developed for underground production blast modelling at the Julius Kruttschnitt Mineral Research Centre (Onederra, 2004b). FRAGMENTO uses a single-ring model to create fractures in near and mid-to-far regions from the blasthole. Onederra (2004b) introduced a stochastic method for simulating coarse fragmentation based on data from an SLC operation. The simulation outputs indicated that, while the generated fragmentation statistics might not be entirely precise, they did exhibit reliable and consistent patterns, especially when forecasting average and maximum particle size values. By comparing these results with real-world case studies, Onederra concluded that FRAGMENTO could be applied in the initial stages of project assessment, such as pre-feasibility and feasibility studies, for the comparison of different drill and blast scenarios and their costs. However, it is important to note the limitations of the simulation approach, associated with the constraints inherent in the single-ring blasting model (Onederra, 2004b).

The Swebrec function and the extended Swebrec function were developed because of differences between the Rossin-Rammler curve and sieved fragmentation data observed in the European Union (EU) 'Less Fines' project, in a collaboration between the Swedish Rock Engineering Research Foundation and Montan Leoben University. The Swebrec function is (Ouchterlony, 2005; Ouchterlony and Sanchidrián, 2018):

$$P_{swe}(x) = \frac{1}{\left\{1 + \left[\ln(x_{max}/x)/\ln(x_{max}/x_{50})\right]^{b}\right\}} \tag{1}$$

where b is the shape parameter, x_{max} is the maximum size of blasted materials, and x_{50} is the median fragment size and x is the fragment size.

The Kuznetsov-Cunningham-Ouchterlony model was developed by replacing the RR function with the Swebrec function in the Kuz-Ram model (Ouchterlony and Sanchidrián, 2018).

More recently, the fragmentation energy-fan model (Ouchterlony et al., 2018) and the distribution-free blast model (Ouchterlony et al., 2017; Sanchidrián and Ouchterlony, 2017) have been developed to predict surface blast PSD. The distribution-free blast model considers various constant parameters that must be defined using experimental data from the site. It is a complex model developed through dimensional analysis, adapted from asteroid collision theory (Sanchidrián and Ouchterlony, 2017). The fragmentation energy-fan describes fragmentation data in the form of percentile fragment sizes as a function of specific charge, represented by a set of straight lines in a log-log diagram. The slope of these fan-shaped lines is related to the percentile passing

of fragments across different sieve sizes, which is used to derive the PSD curve. The constant parameters in these fan-shaped curves should be determined by experimental data (Ouchterlony et al., 2017).

1.2. Numerical modelling of particle size distribution induced by blasting

Numerical modelling in rock mechanics uses mathematical methods to simulate the behaviour of rock masses, treating them as either continuous or discrete systems based on the scale and nature of the problem (Jing, 2003). Previous models have primarily focused on open-pit mining. For example, Ding et al. (2019) used LS-DYNA (ANSYS) to study the damage characteristics of adjacent blastholes after detonation and the distribution of cracks in the damage zone. They generated PSD data from the simulations and used them to optimize blasting parameters (Ding et al., 2019). Another study for open-pit blasting was described in Shahrin et al. (2019), where the discrete element method was used to model the rock media and the bounded particle method was used to implement the detonation pressure and blasthole loading in LS-DYNA. The PSD data were calculated using the GoldSize software (Shahrin et al., 2019).

The Hybrid Stress Blasting Model (HSBM) was developed by the Sustainable Minerals Institute (SMI) of University of Queensland in collaboration with Itasca Consulting Group. The development project was initiated in 2001 and sponsored by a consortium of mining companies and explosive manufacturers, including Dyno Nobel and African Explosives Limited. HSBM is a three-dimensional (3D) blasting model designed to simulate explosive detonation, fragmentation, and blast movement, by integrating various numerical codes to achieve physically realistic outputs. Rock breakage was initially calculated through the 'Blo-Up' component, which utilised Itasca's Particle Flow Code 3D to create a 'synthetic rock mass' with bonds between particles, enabling the model to replicate the macro response of tested rock samples to blast loading. However, the excessive simulation run times, even with supercomputing power, led to the development of 'Blo-Up2', which paired continuum and discrete numerical methods with a fully coupled gas flow model (Ruest et al., 2006; Furtney et al., 2009; Sellers et al., 2012; Onederra et al., 2013; Mitchell et al., 2023). Blastholes were represented using the Fast Lagrangian Analysis of Continua finite difference method, while wave propagation and rock fragmentation for muck pile formation were handled by a bonded lattice model. The explosive in the updated HSBM was represented within the central zones of the Fast Lagrangian Analysis of Continua region using a specialized constitutive behaviour, with detonation models determining key parameters such as the velocity-of-detonation (VoD), the Williamsburg equation-of-state parameters, and the final reaction extent. The near-field region surrounding the explosive was modelled as a Mohr-Coulomb material, which was coupled to the explosive reaction products through the Williamsburg model, ensuring a realistic simulation of the interaction between the detonation process and the surrounding rock mass (Ruest et al., 2006; Furtney et al., 2009; Chitombo et al., 2010; Sellers et al., 2012; Onederra et al., 2013; Mitchell et al., 2023). Despite these advancements, the limitation of the lattice model to simulate stresses or to support complex failure mechanisms has limited its capability. Nevertheless, extensive validation using mine site and laboratory data demonstrated the ability of the original 'Blo-Up' model to simulate microfracture creation through to blast movement. HSBM continues to be used in mining operations to address a range of blasting challenges, though the development of 'Blo-Up2' for the purpose of improving the computational efficiency came with severe limitations. The final report of the HSBM project is documented in (Chitombo et al., 2010).

LS-DYNA (ANSYS) was used to determine the effects of changing the delay time and primer position on particle size distributions in SLC mines. The explosive was modelled using the Jones-Wilkins-Lee (JWL) equation-of-state, and the damage accumulated in the Westerly granite rock was modelled using the Riedel-Hiermaier-Thoma (RHT) material model. To calculate fragment sizes, an indirect method utilising a damage threshold was employed to identify cracks and determine the final fragment sizes. Then the extended Swebrec curve was fitted to the fragment data to create a final PSD curve (Yi et al., 2017). The results showed that longer delay times between blastholes can produce finer fragmentation, and when assessing the impact of primer location, they found more boulders were created at the point of initiation. However, the RHT material model created simulation stability issues due to excessive element distortion, highlighting a challenge when using continuum finite element modelling for simulating fragmentation caused by blasting (Yi et al., 2017). Further research by Yi et al. (2022) with modelling in LS-DYNA determined that increasing the burden dimension will increase the fragment sizes. Then a 3D flow model of the blasted material was constructed in LS-DYNA. For the flow model, the explosive detonation was simulated by a particle blast model, a loose particle model was used to simulate the cave waste rock, a bounded DEM model was used to represent the blasted orebody, and the rock mass around the blast was modelled with a finite element mesh. The particle blast method is an extension of the Corpuscular Particle Method, a coarse-grained, multi-scale approach used for gas dynamics simulation. The results showed that the upper part of the ring has coarser fragments compared with the lower part of the ring and suggest that large fragment sizes and irregular shapes of fragments could cause the gravity flow pattern of fragmented ore to deviate from an elliptical shape. However, to control simulation run times, large particles were used, with waste particle radii ranging from 0.3 m to 0.45 m, and the ore particle radius was 0.24 m. Also, as only a single ring was modelled, blast pre-conditioning of the ring burden was not considered (Yi et al., 2022).

A separate study to reduce the production of boulders in an SLC ring blast. Yang et al. (2021) constructed 2D plane strain models in LS-DYNA to examine the interaction between two blastholes. Image processing using MATLAB was used to segment rock particles in the model. The results showed that shorter delays between holes increased the average and maximum fragment sizes, however, the model had a tendency to create excessively large fragments around the first blasthole to fire. This could be due to a lack of pre-conditioning and representing the rock mass as homogeneous. The study also utilised a 3D single-hole geometry to investigate the effect of using single-versus double-priming. The results show that double-priming can increase the number of fragments and the complexity of the fracture network (Yang et al., 2021).

Zhang et al. (2020) used Particle Flow Code 2D to model the explosive loading by using a particle expansion algorithm and the results were compared with field experiments to calculate the size of the blasting funnel. When an explosive detonates in a rock medium, the explosive energy is absorbed by the rock through plastic deformation and failure. Once the rock can no longer absorb energy completely, surface displacement occurs, leading to rock damage and the formation of a blasting funnel (Zhang et al., 2020). The modelling results showed a good fit for the size of the blast funnel compared to field data. However, there was a clear deviation in the predicted peak particle velocity and blast vibration compared to field data. This discrepancy could be due to

differences in the location of the measured peak velocity in the field and the simulation (Zhang et al., 2020). The software from Lapcevic et al. (2023) encompasses a wide range of blast configurations, including both parallel and fan-shaped blast hole patterns, different explosive types and different rock properties. Additionally, the software can account for blast hole deviation, misfires, and damage caused by previous blasts. The model shows very good agreement with field fragmentation data when blasting in massive rock types with few discontinuities. Fig. 2 shows the 3D fragmentation model setup (Lapčević et al., 2023).

As discussed, all previous models have their own limitations. Within the context of blasting in an SLC operation the main shortcomings of the models are their inability to accurately take into consideration the influence of confinement due to blasting a ring into cave material, and the complex interaction of the detonating explosives and the surrounding rock mass within a blast event.

1.3. Sub-level caving field fragmentation data

Luossavaara-Kiirunavaara Aktiebolag (LKAB) mining company used a camera to take images of blasted material in loaded buckets. Fig. 3 shows a schematic diagram of the camera location for fragmentation monitoring (Wimmer, 2012; Thurley et al., 2015; Manzoor et al., 2022).

Video of more than 15,000 loaded buckets was assessed and a total of 7258 buckets were analysed using a quick rating system written in MATLAB. From the median size of the blasted material in each bucket, they were divided into four categories; fine, medium, coarse and oversize (Thurley et al., 2015; Manzoor et al., 2022). Manzoor et al. (2022) concluded that reducing the diameter of the blastholes did not have a significant impact on the reduction of the median fragmentation size, although the measured blast-induced ground vibration did decrease. However, the effects of blasthole deviation and variations from the design of hole charging on blast performance were not considered (Manzoor et al., 2022). In another study, 3D photogrammetry image data were generated by cameras mounted on Load-Haul-Dump buckets. Bucket sieving was done for about 70 t and the sieving data were compared with the results from the 3D photogrammetry analysis. The results showed that while the size distribution from the analysis did not perfectly match the sieving data, the 3D imaging provided a useful estimation of coarse and fine fragment size fractions. Significant differences were observed between the measurement of the fragment sizes at the drawpoint and the same fragments in Load-Haul-Dump buckets, highlighting the impact of sampling location and the need to measure large quantities of data (Thurley et al., 2015).

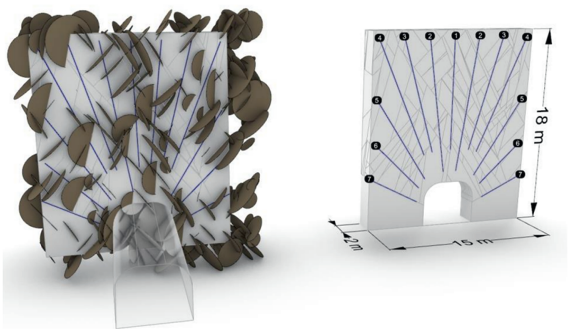

Fig. 2. The 3D fragmentation model illustrating blast ring geometry and design (Lapčević et al., 2023).

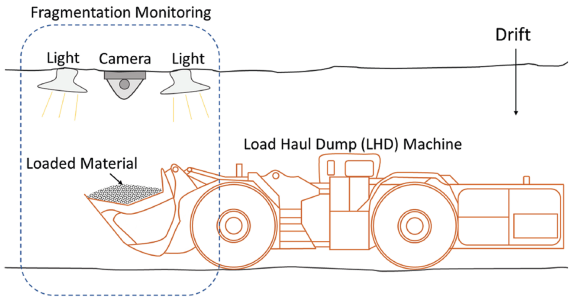

Fig. 3. Schematic of fragmentation monitoring (Manzoor et al., 2022).

Wimmer (2012) used historical data from LKAB mine sites, along with scale model blasting data and laboratory scale data, to examine the flow and breakage behaviours of Kiruna magnetite rocks. The primary conclusion from this work was that magnetite, in terms of fragmentation, exhibited behaviour similar to that of conventional hard rock. This was despite the deviation from the typical Swebrec distribution, which was likely attributed to the internal flow mechanisms within the SLC stope (Wimmer, 2012). In other research the sieving data from Kiruna were compared with the results of the WipFrag 2D image analysis (Wimmer and Ouchterlony, 2009). WipFrag is software that determines PSD data through the processing of muckpile images. The conclusions highlighted several notable drawbacks of image-based fragmentation analysis, specifically issues with the automated delineation of fragments, the impact of image resolution, and material segregation effects (Wimmer and Ouchterlony, 2009). The LKBlast software was developed by LKAB based on the Kuz-Ram model. A comparison study with real case data using image analysis did not reveal a good correlation between the model results and field data. This highlights the difficulty in collecting representative fragmentation data underground and the use of empirical models to predict the size distribution of blasted material (Lith et al., 2004).

At the Ernest Henry Mine (EHM) in Australia, a full-scale experiment was conducted to measure PSD data using a 3D laser scanner at various draw stages corresponding to different extraction tonnages. Additionally, markers were used to examine the flow of blasted material and assess recovery at the draw-points (Campbell, 2019). In some cases, all the scan data for a blast, from its complete extraction at the draw-point, was combined into a single PSD. Analysis of the recorded fragmentation data (Campbell and Thurley, 2017; Campbell, 2019) demonstrated that decreasing the explosive density resulted in coarser particles and increasing the explosive density reduced the fragmentation sizes. In addition, Campbell's work also demonstrated that the ring burden and explosive density have a significant impact on ore recovery. Fig. 4 shows an example of a laser scan image at a drawpoint and its related processing.

In summary, previous research has largely concentrated on open-pit blasting, while studies on underground blasting remain limited. This study developed a model incorporating preconditioning for blasting in sublevel caving and compared its predictions, using similar input variables, with field data available from the literature. The calibrated model accounted for key factors such as confinement, pre-conditioning, delay time, fracture frequency, blast design, and inherent rock properties, offering a more accurate representation than earlier models.

2. Case study

EHM is situated 38 km northeast of Cloncurry within the Eastern Fold Belt of the Mount Isa Inlier in northwest Queensland

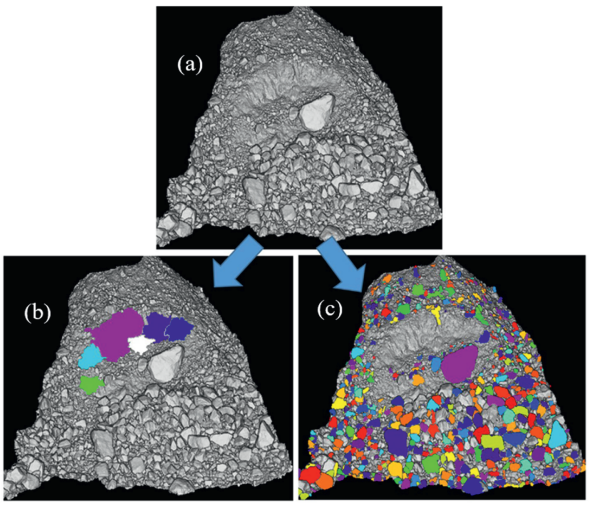

Fig. 4. Illustration of a laser scan and particle segmentation: (a) Processed scan, (b) regions containing fines coloured, and (c) individual, non-overlapping particles coloured (Campbell and Thurley, 2017).

(Campbell, 2019). EHM is an active SLC operation below an old open pit. SLC production commenced after the completion of the open pit and targets ore situated nearly 1000 m deep, as illustrated in Fig. 5 (Campbell, 2019).

Table 1 outlines the typical ring design parameters for the SLC operation at EHM. Each ring requires 165 m of drilling and contains approximately 2850 t of rock. Table 2 presents the rock properties for the Volcanic ore. Campbell's study assessed the impact of different explosive densities (0.9 g/cc, 1.1 g/cc, and 1.25 g/cc), burden sizes (2.2 m, 2.6 m, and 3 m), and hole diameters (89 mm, 102 mm, and 114 mm) on fragmentation, flow characteristics and the recovery of blasted ore (Campbell and Power, 2017; Campbell and Thurley, 2017; Campbell, 2019).

The EHM orebody is a breccia formation within Proterozoic rocks, which are covered by a 50-m-thick layer of sand, clay, shale, and gravel (Fig. 6). Above the intermediate volcanic rocks that host the orebody, the hanging wall sequence includes a shear zone, Schist, fine-grained Albitite, and Diorite (Campbell, 2019).

3. Methodology

Numerical modelling was employed in this study to examine the effects of rock properties and blast-induced fragmentations. A prior study by Khodayari et al. (2024) simulated rock fragmentations using various explosive densities, joint set spacings, and burden sizes. Built on this work, this study expanded the scope by incorporating additional blast design parameters and a wider range of rock properties. PSD curves were generated from numerical simulations and subsequently used as inputs for regression analyses to develop the new regression predictive model.

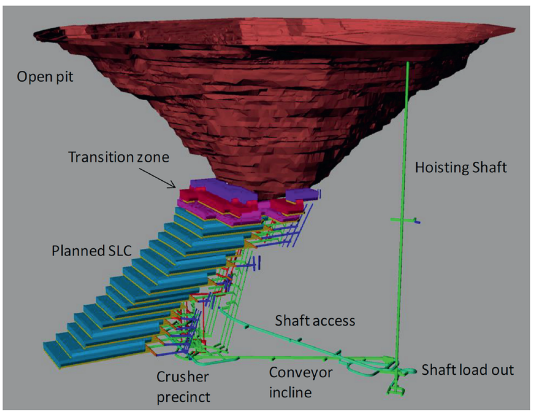

Fig. 5. The mining layout of the EHM (Campbell, 2019).

Table 1
Ring blast design parameters.

Parameter	Value
Borehole diameter (mm)	102
Burden (m)	2.6
Number of holes per ring	8
Explosive density (g/cc)	1.1
Delay time (ms)	25
Powder factor (kg/t)	0.4

Table 2
Rock properties.

Rock type	Felsic volcanic ore
Density (g/cc)	3.83
Young's modulus (GPa)	66.7
Poisson's ratio	0.27
P-wave velocity (m/s)	4665
S-wave velocity (m/s)	2618
UCS (MPa)	193.8
Tensile strength (MPa)	9.2
Fracture frequency (fractures/m)	2

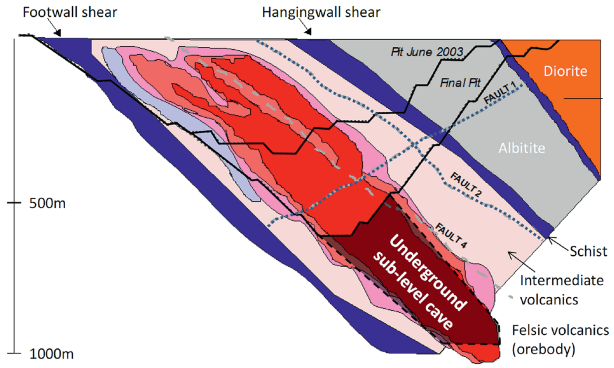

Fig. 6. General geology of EHM.

3.1. Numerical simulations

The Mechanistic Blasting Model (MBM) is used to simulate the explosive loading applied to a blasthole wall and the subsequent fracturing of the surrounding rock masses (Minchinton and Lynch, 1997; Minchinton and Dare-Bryan, 2005; Dare-Bryan et al., 2013). MBM is built on the commercial hybrid finite element/discrete element code Elfen (Owen et al., 1992), utilising proprietary Orica modules to simulate the detonation of the explosive charge in a blasthole, including gas loading of the surrounding rock masses. The non-ideal detonation data was used to model the reactive flow of the detonation products, both before and after the sonic Chapman-Jouguet plane, and also the effects of rock confinement and blast hole diameter on the resulting velocity-of-detonation (VoD) and the pressure-time profile on the blast hole wall (Kirby et al., 2014).

Although MBM is a comprehensive 3D model, practical computational constraints arise when running 3D models due to the size of the model that can be simulated and the complexity of fracturing in three dimensions. As a result, the majority of simulation projects currently are two-dimensional, in axisymmetric or plane strain configurations.

In this study, the ring blasts were simulated using a plane strain 'plan view' model, which takes a horizontal section through the ring. In the software, while the wave dispersion is accurate due to holes being modelled as circles, the lack of S-waves radiating from the holes is a limitation. However, the implementation allows modelling of inter-hole interaction to evaluate blast patterns and timing.

The design parameters and rock properties of EHM listed in Tables 1 and 2 were used to prepare the baseline simulation in this work. The EHM blast design is shown in Fig. 7. The holes in Fig. 7 are labeled A to H and the numbers show the detonation sequence of holes, where charges with the same number have the same initiation delay Therefore, the detonation sequence starts with hole 1, followed by hole 2, and then proceeds with the two holes numbered 4, the two holes numbered 6, and finally the two holes numbered 8. The broken green line in Fig. 7 represents the horizontal section through the ring, which was used to construct the 'plan view' model geometry (Fig. 8). This section was selected because it represents the average charge spacing within the ring design and so will generate an 'average' fragmentation for the ring. The model geometry used a generalized representation of existing jointing within the rock mass as a discrete fracture network, based on the fracture frequency (Table 2).

The level of confinement due to the cave material, for the ring to blast into, is a key parameter that must be addressed in the model. The optimal way to represent this confinement needs to be investigated. The initial baseline model consisted of three rings, of which only the first two were fired. Additionally, a void was created in front of the first ring to allow the movement of blasted material following the firing of the first ring. Fig. 9 illustrates the variability in damage after the first ring has been fired due to different existing fractures between holes. The damage from the first ring has pre-conditioned the front half of the second ring burden. Subsequently, the second ring fires into the partially confined first ring burden, simulating the confined ring blasting conditions within an SLC operation. The numerical results used in our analysis are from the second ring.

In-situ stress keeps the fracture surfaces in contact during explosive loading, which can lead to more consistent results in the simulations. In-situ stresses were applied as a face loading of

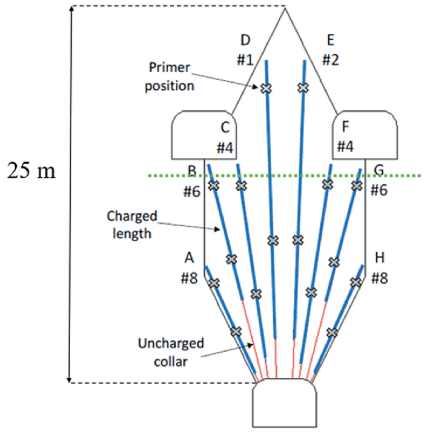

Fig. 7. Blast design of EHM (Campbell and Thurley, 2017).

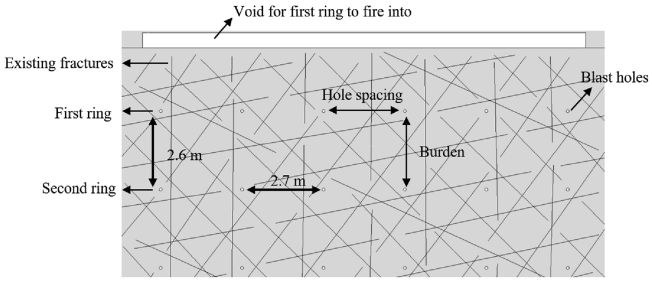

Fig. 8. Baseline model geometry with the same delay time as used in EHM blast design.

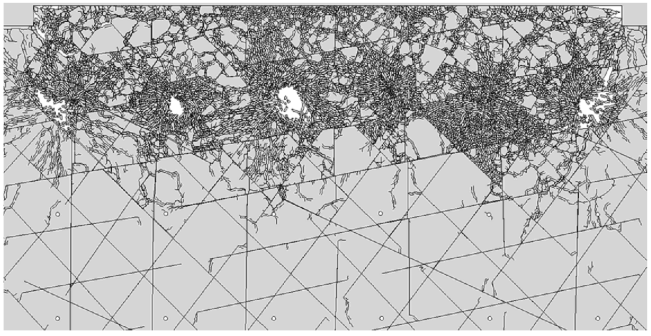

Fig. 9. Simulation after the first ring has fired.

1 MPa to the top and bottom of the geometry outer boundary, while a loading of 2 MPa was applied to the left and right sides of the outer boundary. While these are not very high stresses, the stress field local to the ring will be lower than the natural stresses at this depth due to the influence of the cave.

After detonating the second ring, a region was sampled using the FragSize software which delineates all the fragments and creates a cumulative size distribution (Dare-Bryan et al., 2013). The height of the region matches the burden, and its width is the distance between the first and last hole (Fig. 10).

3.2. Calibration and verification of the Mechanistic Blasting Model (MBM)

To verify the numerical model, its results were compared with the measured fragmentation data from EHM. In the EHM dataset, 125 measurements were conducted at various increments through the excavation at the draw points. Scans were taken every 250 t up

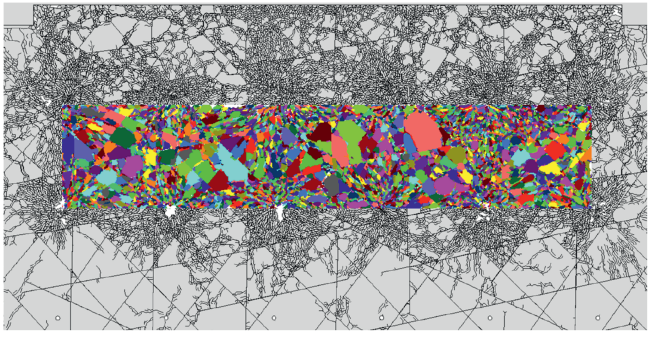

Fig. 10. Simulation after the second ring has fired, showing the second ring burden region sampled for fragment size analysis.

to 1000 t and then every 500 t until the prescribed draw was reached, helping to reduce bias in size distribution calculations. To ensure an unbiased calculation of particle sizes, Campbell used a combined dataset created by merging the fragmentation data from all scans into a single dataset for each draw point (Campbell, 2019).

The most accurate measurement of the size distribution of broken rocks is through sieving the material. However, sieving is rarely used due to its high cost and disruption to mining operations, particularly in underground mining. In the EHM study work, only the remote laser scanning measurement method was used. Since laser scanners can only capture the surface of the muckpile at the draw-point, the dataset produced will be biased as the 3D information is not available. The combined dataset based on different draw tonnages from the stope as discussed above helps minimise any bias, though it cannot be eliminated. It is also well known that remote methods have limitations in capturing fines (Sanchidrián et al., 2009; Noy, 2013; Thurley, 2013). However, in Campbell's dataset, the proportion of fines (particles smaller than 50 mm) is less than 10 % (Campbell, 2019), therefore, the use of P20 as the smallest percent passing data point is reasonable.

The EHM measured fragmentation data covers blast design changes with explosive densities of 0.9 g/cc, 1.1 g/cc and 1.25 g/cc, burden sizes of 2.2 m, 2.6 m and 3 m, and hole diameters of 89 mm, 102 mm and 114 mm. All these scenarios were modelled in this study. Non-ideal detonation modelling was used to generate detonation parameters for the range of hole diameters, explosive density and explosive types (Kirby et al., 2014). The non-ideal detonation model uses unconfined velocity-of-detonation measurements over a range of charge diameters, and the product critical diameter, to characterise the reaction kinetics within the model and fit an unconfined velocity-diameter curve to the measured data. Fig. 11 shows examples of the unconfined velocity-diameter curve fitted to measured data for a heavy ANFO and a straight emulsion (Subtek™). Note the higher sensitivity of the straight emulsion enables the product to detonate unconfined in much smaller diameter charges than the heavy ANFO, which corresponds to a higher confined VoD for a given hole diameter. Further details can be found in (Kirby et al., 2014).

Titan™ 7000i emulsion was used for the different blasting scenarios at EHM. The Subtek™ product from the CPeX library was selected as representative of Titan™ 7000i. The non-ideal detonation data for Subtek™ are shown in Table 3. The table shows that increasing explosive density has a greater impact on the velocity-of-detonation (VoD), and detonation pressures than increasing the hole diameter. The Chapman-Jouguet density (CJ Density) only has incremental increases across the range of hole diameters modelled. While the numerical modelling requires the pressure-time detonation data of non-ideal detonation, for completeness, it is worth noting that from the ideal detonation calculations, the effective detonation energy released for explosive densities of 0.9 g/cc, 1.1 g/cc and 1.25 g/cc to be 1.86 MJ/kg, 2.16 MJ/kg and 2.38 MJ/kg, respectively.

The reported EHM dataset includes the 20%, 50%, and 80% passing sizes (P20, P50, and P80), along with the maximum particle size from each blast. To predict particle size variations based on the field data, an appropriate distribution function was needed. The Rosin-Rammler, Gates-Gaudin-Schumann (GGS) and Swebrec functions were explored for their representation of the fragment size distribution of the baseline EHM data (Table 4), as shown in Fig. 12.

Clearly, the Swebrec and Rosin-Rammler distribution functions fit the field data better than the GGS function, especially for coarse size fractions. Both the Swebrec and Rosin-Rammler distribution functions are suitable candidates. The Swebrec function was chosen in this study due to the increased flexibility of its three parameters over the two in the Rosin-Rammler function.

Fig. 13 compares three raw MBM PSD curves, corresponding to void sizes of 50 cm, 25 cm, and 10 cm, with the baseline Swebrec curve. The MBM curves for 50 cm and 25 cm void sizes are similar and are significantly finer compared to the measured data. However, the curve for the 10 cm void size aligns well with the measured data for the coarser size fractions. Therefore, the measured baseline Swebrec curve is taken as the Swebrec curve fitted to the raw MBM PSD data. Note that the humps in the raw PSD curves from the numerical models are artifacts of the mesh dependencies in the numerical models. The mesh size used in the model dictates the minimum size of the modelled fragments, which causes a bias at the size of 50 mm in these simulations.

The coarser fragmentation with the smaller void size highlights the influence of confinement in blast performance. While it is difficult to exactly replicate the confinement against a burden in a SLC ring blast in numerical simulations, changing the void size in the MBM geometries is an effective means of calibrating the model against the measured field data.

Fig. 14 compares the Swebrec curves fitted to the measured EHM fragmentation data and the raw simulation PSD data for different explosive densities. The model reasonably replicates the changes in fragmentation for the coarse size fractions with different explosive densities. However, for the 1.25 g/cc explosive density the model predicts a finer fragmentation size in the medium size fraction range as shown by the red broken line Swebrec curve compared to the broken green line fitted to the field data. Despite this, the overall agreement between the model outputs and EHM data gives reasonable confidence in the numerical models.

When comparing the model results to the field data for the three burden sizes (Fig. 15) they all produced similar P80 passing sizes. However, in the fines portion of the PSD, the measured data

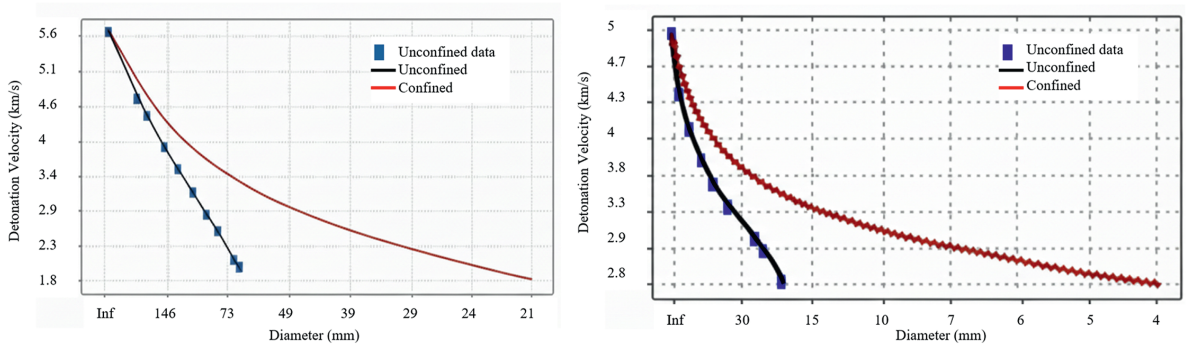

Fig. 11. VoD vs diameter curves for unconfined measurements and model data for (a) a heavy ANFO and (b) Subtek™.

Table 3
Non-ideal detonation data for Subtek™.

Hole diameter (mm)	89			102			114		
Explosive density (g/cc)	0.91	1.13	1.25	0.91	1.13	1.25	0.91	1.13	1.25
VoD (m/s)	4691	5376	5750	4732	5433	5815	4761	5476	5866
vN pressure (GPa)	10.01	14.19	16.47	10.21	14.55	16.92	10.35	14.83	17.27
CJ pressure (GPa)	4.97	7.73	9.24	5.07	7.93	9.49	5.14	8.08	9.68
CJ density (g/cc)	1.18	1.42	1.55	1.19	1.43	1.56	1.18	1.44	1.58
CJ time (μs)	4.21	4.86	5.21	4.37	4.82	5.07	4.86	4.97	5.03

Table 4
Fragmentation data for a range of explosive densities measured at EHM (after Campbell, 2019).

Percent passing (%)	Passing size (mm)		
	Explosive density1.1 (g/cc) (Baseline)	Explosive density 0.9 (g/cc)	Explosive density 1.25 (g/cc)
20	94	111	84
50	216	235	196
80	393	437	350

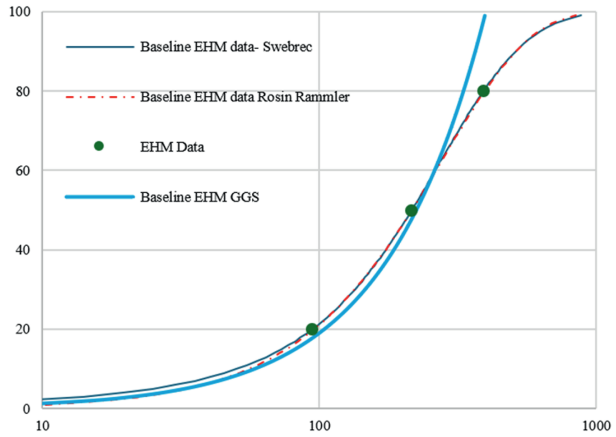

Fig. 12. Comparison of different distribution functions fitted to field data measured for the baseline EHM blast design.

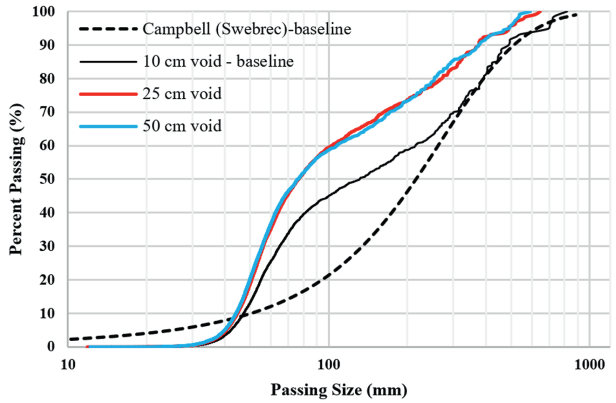

Fig. 13. Fragmentation from baseline simulations with a range of void sizes compared to the baseline data of Campbell (2019).

for the smaller 2.2 m burden was coarser than the baseline (with a 2.6 m burden), while, as one would expect the 2.2 m burden model created finer fragmentation than the baseline. The unexpectedly coarser measured fragmentation for the 2.2 m burden size could be due to the excessive preconditioning from the previous ring.

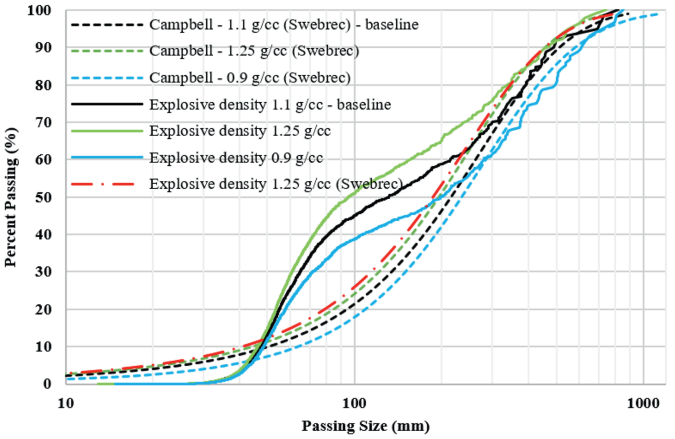

Fig. 14. Comparison of the measured fragmentation curves fitted to blast field data (Campbell dashed lines) with the raw simulation PSD outputs (solid curves) for explosive densities 0.9 g/cc, 1.1 g/cc, and 1.25 g/cc. The red chain curve shows the Swebrec curve fitted to the raw PSD output for explosive density 1.25 g/cc.

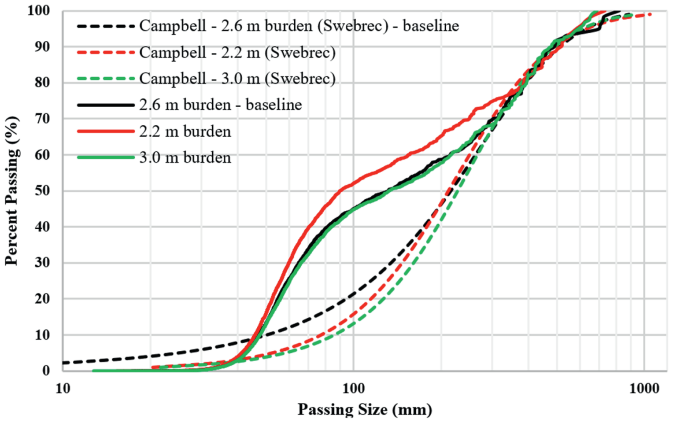

Fig. 15. Comparison of the PSD curves for blasts with different burden sizes.

This preconditioning would impact the explosive/rock interaction after excavation of the previous ring, which is not currently considered in the numerical model. Another possibility could be that the burden of 2.2 m mobilizes more cave material, resulting in

coarser fragments at the draw point. As for the 3.0 m burden size, the model resulted in slightly coarser fragmentation compared to that of the 2.6 m burden size, whereas in the field data, the 3.0 m burden case exhibited significantly coarser fragmentation in the fines portion of the PSD.

Comparing the raw PSD simulation data for the range in blast hole sizes modelled (Fig. 16), the change in PSD follows a pattern similar to the changes in explosive densities (Fig. 14). As Campbell mentioned, changing the explosive density to 0.9 g/cc and 1.25 g/cc in 102 mm blast holes produces a similar energy distribution to that of 89 mm and 114 mm blast holes with an emulsion density of 1.1 g/cc (Campbell, 2019). Therefore, the measured fragmentation Swebrec curves for different explosive densities have been overlaid on the raw simulation PSD curves for different hole diameters, with reasonable agreement (Fig. 16).

In summary, after calibrating the model geometry to an appropriate confinement with the 10 cm void MBM can effectively predict the coarse portion of the blast induced fragmentation and a fitted Swebrec curve can provide a full PSD for the simulations.

4. Results and discussion

The initial comparison between the model results and the EHM measured fragmentation data, as reported by Khodayari et al. (2024), demonstrated a strong correlation, especially for fragmentation sizes larger than P65. In Figs. 14–16, the simulation outputs for cases with different explosive densities, burden sizes, and hole diameters closely match the Swebrec curves fitted to the EHM data for fragmentation sizes greater than P70. Following this, multiple scenarios were simulated using MBM, incorporating varying input parameters related to the rock properties and blast design, to assess their effects on the resulting particle size distributions. A key contribution of this study, compared to the work by Khodayari et al. (2024), lies in its expanded scope. While Khodayari et al. focused on the effects of explosive densities, burden sizes, and joint set spacings, this study further investigates additional factors, including different hole diameters, in-situ stresses, tensile strength, and charge spacing, to evaluate their impact on the size distribution of blasted materials. Swebrec curves were fitted to the raw MBM fragmentation data. The fitted curves were then used to produce passing size data for P20, P50 and P80 for regression analysis. The identification of input parameters that have the greatest influence on fragmentation led to the derivation of regression predictive models. To assess the performance of the new regression models, the coefficient of determination (R^2) was used.

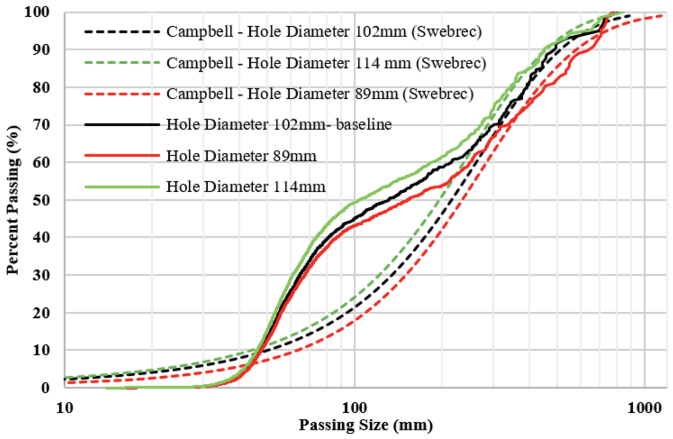

Fig. 16. Comparison of the PSD curves for blasts with different hole diameters.

The input variables for the numerical simulations are shown in Table 5. The non-ideal detonation parameters described in Table 3 were included for the relevant changes to blasthole diameter and explosive density. A total of 34 model scenarios were simulated in MBM, changing one input parameter at a time, as well as combinations of parameters.

Table 6 presents the passing size data across all 34 modelled scenarios. The names of model scenarios reflect the parameters that have changed compared to the baseline model, as discussed above. For instance, TS 5 represents that only the tensile strength has been altered from 9.2 MPa to 5 MPa, compared to the baseline model.

4.1. Definition of rock property and blast design factors

The different input parameters (Table 5) were divided into four groups of variables. The first group, Blast Design Factors (BDF), includes parameters that can be controlled by operators. These parameters are charge spacing, burden, hole diameter, and explosive density. According to Table 6, an increase in charge spacing and burden sizes leads to larger fragment sizes, while an increase in hole diameter and explosive density results in smaller fragment sizes. Thus, the BDF is defined as

$$BDF = \frac{CS*B}{ED*HD} \tag{2}$$

where the variables are defined in Table 5.

Note that BDF is directly related to powder factor. However, powder factor represents the average explosive charge density for the entire blast ring, not the variations of the charge density within the ring. Therefore, BDF is used instead powder factor to differentiate the contribution of the range of blast design parameters modelled.

The second group of parameters affects the quality of the rock mass. The Rock Property Factor (RPF) is defined by variations in size distributions due to changes in tensile strength and fracture densities. According to Table 6, an increase in tensile strength leads to larger fragment sizes across all models. Table 6 also shows that the effect of fracture density on P80 differs from its effect on P20 and P50. With fewer discontinuities in the rock mass, the blast produces finer fragmentation below 80% passing compared to the baseline case. This finer fragmentation occurs because stress waves radiating from each charge experience less disruption, maintaining higher amplitude as they travel further through the rock mass. Consequently, different definitions of RPF are required. RPF for P80 is defined in Eq. (3), while RPF for P20 and P50 are defined in Eq. (4):

$$RPF_{P80} = TS/FD \tag{3}$$

$$RPF_{P50 \text{ and } P20} = \text{TS*FD} \tag{4}$$

The third category is In-situ stress (IS), which relates to stresses in the rock mass in the ring due to the influence of the excavation on the background stress field and is presented in MPa. According to Table 6, for the range of stresses considered, increasing in-situ stresses leads to a decrease in fragment sizes. The fourth category comprises non-ideal detonation parameters, to determine the influence of different detonation characteristics on fragmentation. Since the type of explosive was the same across the models, the Non-Ideal Detonation Factor was not considered in the regression analysis. However, non-ideal detonation parameters will be investigated further in future research, when different types of explosives are considered.

Table 5
The input variables.

Input parameter name	Abbreviation	Unit	Parameter variations
Hole diameter	HD	mm	89, 102 and 114
Explosive density	ED	g/cc	0.9, 1.1 and 1.25
In-situ stress	IS	MPa	1, 5 and 10
Burden	B	m	2.2, 2.3, 2.4, 2.6, 2.8, 2.9 and 3
Tensile strength	TS	MPa	2.5, 5, 9.2, 15, 20, 25 and 30
Fracture density	FD	Joints per m	1, 2 and 4
Charge spacing	CS	m	2.1, 2.3, 2.5, 2.7 and 2.9

Table 6
Different model scenarios and their resulting passing size data.

Scenario name	Model number	P20 (mm)	P50 (mm)	P80 (mm)
TS 5	Model 1	40.78	130	282.05
TS 2.5	Model 2	22.22	90	230.68
Burden 2.4	Model 3	62.7	171	343.18
Burden 2.9	Model 4	87.76	208	382.85
IS 10	Model 5	43.21	140	312.64
IS 5	Model 6	67.61	175	343.84
DI 89	Model 7	97.17	235	431.25
DI 114	Model 8	55.81	160	332.42
DI 89 ED 0.9 TS 5	Model 9	105.41	238	423.32
DI 89 ED 0.9 TS 20	Model 10	117.66	254	443.53
DI 114 ED 0.9	Model 11	80.23	209	402.29
DI 114 ED 1.25	Model 12	49.14	150	317.82
DI 89 ED 1.25	Model 13	78.86	190	357.50
One joint per m	Model 14	46.63	162	374.47
TS 15	Model 15	96.21	220	394.81
TS 20	Model 16	108.14	249	447.9
TS 25	Model 17	115.34	260	461.93
TS 30	Model 18	163.44	350	599.65
Burden 2.2	Model 19	51.77	154	324.58
DI 89 ED 0.9	Model 20	111.28	244	430.53
DI 89 ED 0.9 TS 20 IS 10	Model 21	111.92	250	441.30
DI 89 ED 0.9 TS 30 IS 10	Model 22	195.31	342	507.79
DI 89 ED 1.25 TS 20 IS 10	Model 23	86.21	218	407.4
DI 89 ED 1.25 TS 30 IS 10	Model 24	148.36	330	585.3
ED 0.9	Model 25	110.97	243	429.31
ED 1.25	Model 26	78.84	187	346.18
Spacing 2.5	Model 27	65.75	180	359.7
Spacing 2.9	Model 28	85.76	207	388.02
Baseline	Model 29	82.42	200	374.32
Burden 2.3	Model 30	60.25	161	320.68
Burden 3	Model 31	101.22	221	390.71
Four Joints per m	Model 32	89.85	203	365.55
Spacing 2.1	Model 33	51.6	150	309.08
Spacing 2.3	Model 34	58.05	160	323.15

4.2. Regression analysis

A multivariate regression analysis was performed on most of the data listed in Table 6, as training data, to identify key parameters influencing the PSD in SLC operations and to formulate a prediction equation. Fig. 17 presents scatter plots illustrating the relationships between selected P20, P50, and P80 size data and the explanatory variables. The figure reveals a strong linear relationship between the percentage changes in input variables and the passing size data, with simple least-squares fittings yielding an R^2 value greater than 80% for all variables.

4.2.1. Prediction of P80, P50 and P20 passing sizes

For P80, a sensitivity analysis was performed using the *t*-statistic (t) and *p*-value. The *t*-statistic is used to determine the significance of each regression coefficient, while the *p*-value indicates the probability of obtaining a *t*-statistic as extreme as the one calculated from the data, assuming the null hypothesis is true. In this case, the null hypothesis assumes that the corresponding regression coefficient has no effect on the P80 prediction. A low *p*-value suggests that the coefficient significantly contributes to the model, indicating that the associated parameter has a meaningful impact on P80. (Greenland et al., 2016).

Table 7 shows the significance levels based on *p* values. Variables with a *p*-value of less than 0.05 are generally considered sensitive. Each parameter *p*-value is categorised into five significance levels: highly significant, significant, mostly significant, marginally significant, and low significance. Additionally, a parameter is considered sensitive if the $t \geq 1.3$ or $t \leq -1.3$.

Table 8 presents the results of the regression analysis, highlighting variations in *p*-values. The table identifies the most sensitive variables affecting the P80 passing size. According to Table 8, RPF is the most significant parameter, while IS is the least significant parameter. It should be noted that the sensitivity analysis results indicate that the P80 is sensitive to all three input variables: BDF, RPF_{P80}, and IS.

Fig. 18 displays the standardised coefficients of the predictor variables. The standardised coefficients are obtained if the

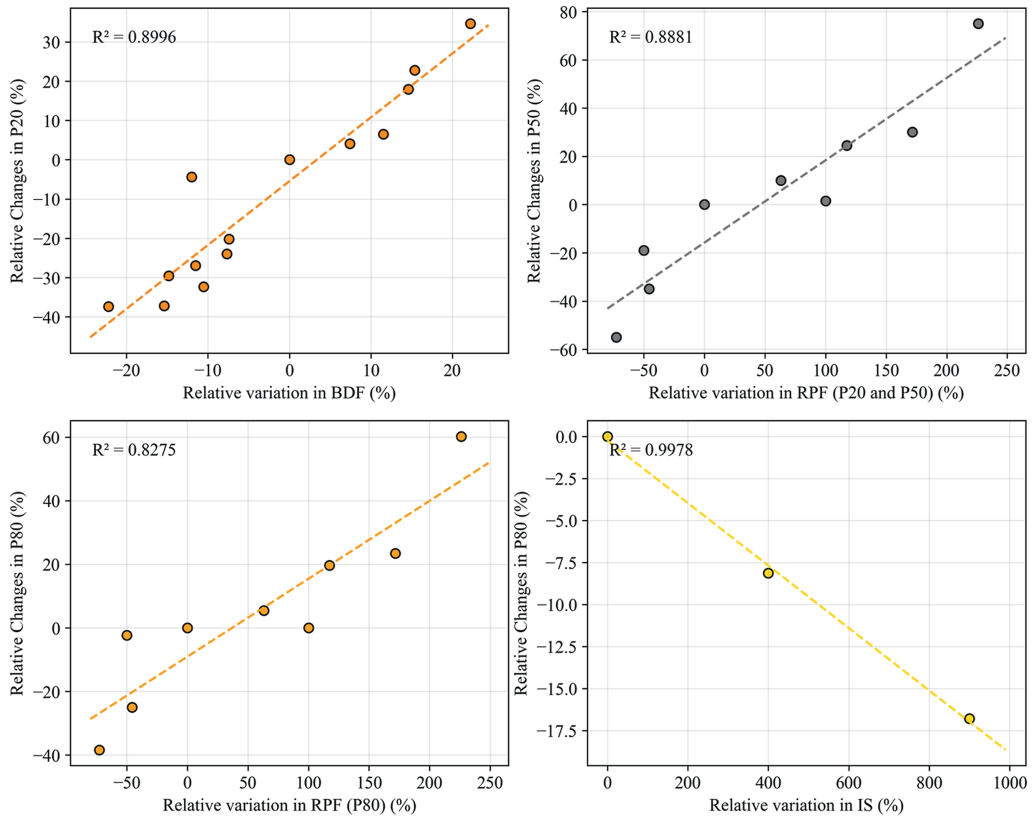

Fig. 17. Sensitivity analyses of P20, P50 and P80 against the BDF, rock property factor and in-situ stresses.

Table 7
p-value significance code.

p-value range	Significance
$0 < p < 0.001$	Highly significant
$0.001 < p < 0.01$	Significant
$0.01 < p < 0.05$	Mostly significant
$0.05 < p < 0.1$	Marginally significant
$0.1 < p < 1$	Low significant

Table 8
Sensitivity analysis for the P80 passing size.

Variable	*p*-value	Significance codes
BDF	0.001	Highly significant
In-situ stress	0.07	Mostly significant
Rock property factor P80	<0.001	Highly significant

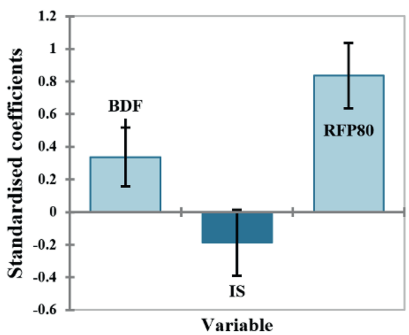

Fig. 18. P80 Standardised coefficients (95% confidence interval).

regression analysis is repeated with standardised response and predictive variables. That is, each variable has its mean subtracted, and the deviations from the mean are then divided by its sample standard deviation. These standardised coefficients are directly comparable and indicate the relative importance of the predictor variables on the response. The lines at the ends of the bars in the figure represent the 95% confidence intervals for these coefficients. The analysis finds that increasing in-situ stress has a decreasing effect on the P80 passing size. This is counter to expectations. It is theorised that the while higher in-situ stresses are sufficient to keep the in-situ discontinuities tightly closed, aiding blast-induced stress wave transmission in the rock, they are not sufficient to arrest fracture creation and propagation. In contrast, RPFP80 and BDF have an increasing effect on fragmentation size, with larger values for these variables resulting in larger fragments.

To predict P80 using the three variables, the R^2 value was 0.79. Among all the parameters, RPF_{P80} and BDF were the most influential, having a significant positive impact on fragment size.

Based on the regression analysis, P80 can be predicted as

$$P80\ (mm) = 135.17 - 4.46IS + 2347.81BDF + 17.35RPF_{P80} \tag{5}$$

The standardised residuals (observation less model fitted value) for the model used to predict P80, are shown in Fig. 19. The residuals have a mean of zero, a consequence of the least squares fitting algorithm, and the standardised residuals are the residuals divided by their standard deviation. If standardised residuals have no obvious pattern and lie between −2.6 and 2.6, which includes 99% of a standard normal distribution, the model is generally considered to be a reasonable fit to the data. In this case, and for the other prediction models, all the standardised residuals lie within these limits.

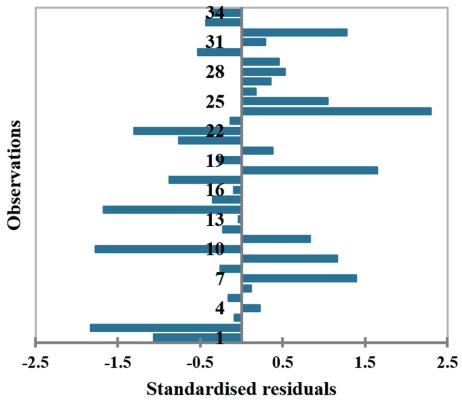

Fig. 19. Standardised residuals for the regression model predicting P80.

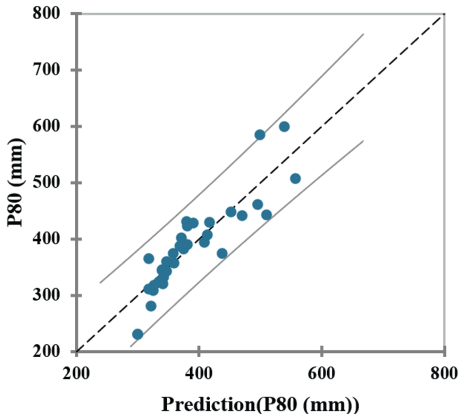

Fig. 20. Scatter plot of P80 vs predicted P80.

Fig. 20 shows a scatter plot which compares the observed P80 values with the predicted P80 values from the multivariate linear regression model. The dashed line indicates the line of perfect prediction, and the solid lines represent confidence interval of 95%. The clustering of data points around the dashed line indicates a good fit of the model, with a weighting of predictions near the actual values. A few data points lie close to the solid lines and correspond to the very high tensile strength (30 MPa) and low tensile strength (2.5 MPa) models. While the new regression model can predict P80 with good accuracy, it should be further evaluated for cases of very high and very low tensile strengths in future applications.

The methodology for predicting P20 and P50 passing size data was similar to that used for predicting P80. Multivariate regression analysis was employed to develop equations for P20 and P50 based on BDF, RPF, and IS. The only difference was in defining the RPF. As shown in Table 6 and defined in Eqs. (3) and (4), the RPF for P80 differs from that for P20 and P50 due to the varying effects of increasing fracture density on these percent passing values. Despite the revised equation for the RPF for P50 and P20 compared to P80, the RPF still has the greatest significance for P50 and P20 passing sizes (Table 9). The standardised coefficients for variables impacting P50 and P20 (Fig. 21) shows that the trends for RPF, DBF and IS are the same as P80 (Fig. 18).

The equations for predicting P20 and P50, with R^2 values of 0.87 and 0.85, respectively:

$$P20\ (\text{mm}) = -59.64 - 2.11IS + 1548.30BDF + 1.95RPF_{P20\text{ and }P50} \quad (6)$$

$$\text{P50}\ (\text{mm}) = -10.04 - 3.52IS + 2186.36BDF + 3.26RPF_{P20\text{ and }P50} \quad (7)$$

Fig. 22 presents scatter plots illustrating the relationship between the predicted P20 and P50 values and those derived from the fitted curves based on simulation results. Compared to the P80 model, the data points for the P50 and P20 models are more closely clustered within the confidence intervals, indicating higher model accuracy for predicting P50 and P20. This is further supported by the respective R^2 values, being greater than for the P80 model.

In Fig. 22, the data points close to the solid lines correspond to models with very high and very low tensile strength, as with the P80 model. This indicates that all the regression models are less reliable at the extreme tensile strengths modelled. However, it should be noted that, based on all the scatter plots and R^2 values, overall, the proposed models predict the size distribution well.

4.2.2. Validation of the derived predictive PSD models

For a range of scenarios, including the baseline scenario and those with explosive densities of 0.9 g/cc and 1.25 g/cc, as well as that with a burden size of 3.0 ms, Figs. 23–26 compare three sets of results: the EHM measured data, predictions from the derived models (Eqs. (5)–(7), referred to as the "new regression model" in these figures) and the Swebrec curves fitted to the MBM simulation outputs (referred to as "simulation" in these figures). The MAPE between the models and the EHM data are also provided.

For the baseline configuration, Fig. 23 presents only two curves, as the field measurement Swebrec curve was taken as the fit of the Swebrec function to the raw MBM curve. The MAPE for the new regression model increases from less than 10% at P80 to more than 25% at P20 when compared to the field data for the baseline configuration.

Fig. 24 shows a comparison of the two models and EHM data for the 1.25g/cc explosive density design change. The maximum MAPE between the numerical model and EHM data is 7% while that between the new model and EHM data is 26%.

For the 0.9 g/cc explosive density design change, comparisons between both model PSDs and EHM highlight a much better prediction, with maximum MAPE values being less than 5% for MBM and 10% for the new model (Fig. 25).

Fig. 26 shows the PSD comparisons for the 3.0 m burden design. The maximum MAPE values are 20% for MBM and 22% for the new regression predictive model at P20. As previously mentioned, there was a significant deviation from the predicted fines portion of the PSD curve compared to the measured data across the range of burdens analysed. This variation will naturally translate into the new regression model, as it was trained off the MBM data. Despite this, the simulation prediction of field data remains reasonable.

In all size distributions, the MAPE for the simulation is lower than that for the new regression predictive model, indicating that the simulation offers better accuracy in predicting various fragment sizes. Both the MBM and new empirical model are the most accurate at predicting P80. As demonstrated in Figs. 13–16 and discussed in previous sections, it is evident that MBM provides better predictions for larger fragment sizes compared to smaller ones. Overall, the new empirical model provides reasonably good predictions for P20, P50 and P80, with the maximum MAPE value across all cases being 30%.

To further assess the performance of the derived regression models, two additional simulations were conducted, with several parameters adjusted from the baseline model (Tables 1 and 2).

For the first blast (NB1), the hole diameter was changed from 102 mm to 89 mm, the explosive density was increased from 1.1 g/

Table 9
The sensitive parameters on P50 and P20.

Variable	P50		P20	
	P-value	Signification codes	*P*-value	Signification codes
BDF	<0.0001	Highly Significant	<0.0001	Highly significant
In-situ stress	0.02	Mostly significant	0.02	Mostly significant
Rock properties factor for P50 and P20	<0.0001	Highly Significant	<0.0001	Highly significant

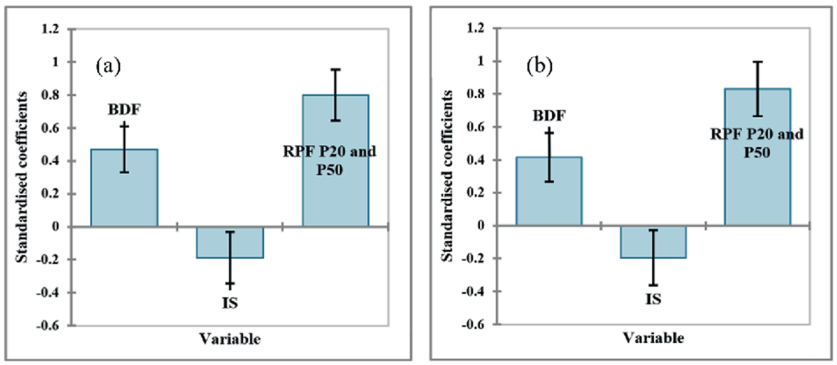

Fig. 21. (a) P20 standardised coefficients at a 95% confidence interval and (b) P50 standardised coefficients at a 95% confidence interval.

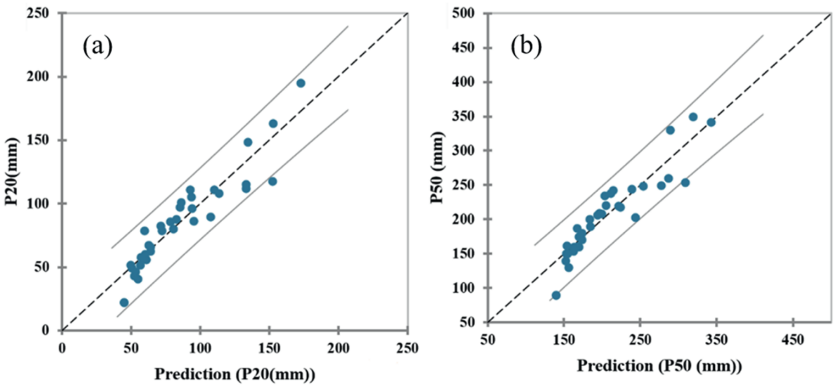

Fig. 22. Scatter plot of (a) P20 vs predicted P20 and (b) a scatter plot of P50 vs predicted P50.

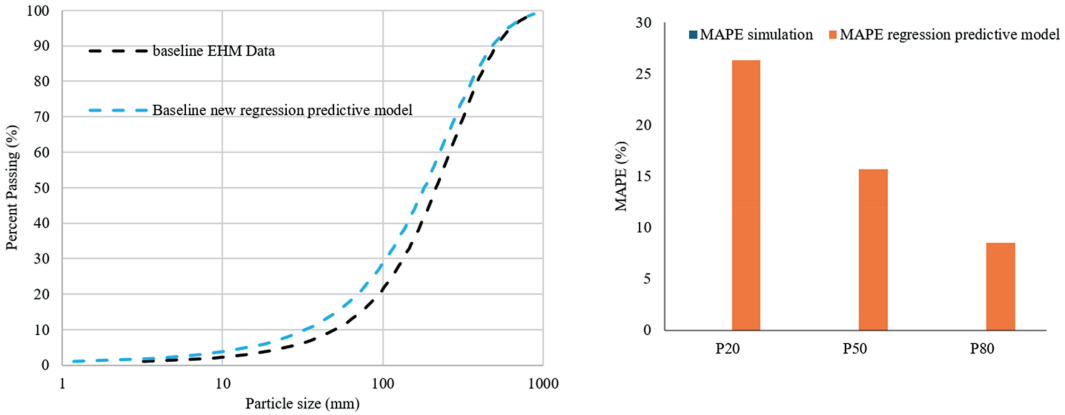

Fig. 23. Comparison of PSD curves for the EHM measured data (and MBM simulation) and the new regression predictive model, for the baseline configuration.

cc to 1.25 g/cc, the tensile strength was increased from 9.2 MPa to 20 MPa, and the in-situ stress was increased from 1 MPa to 5 MPa. For the second blast (NB2), the hole diameter was changed from 102 mm to 114 mm, the explosive density was modified from 1.1 g/cc to 0.9 g/cc, and the tensile strength was increased from 9.2 MPa to 20 MPa. For these two cases, the predicted P20, P50 and P80

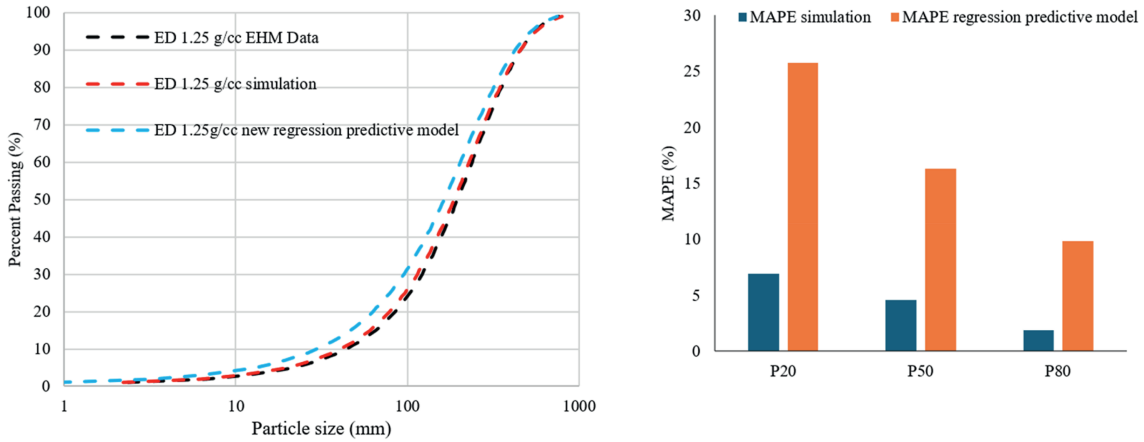

Fig. 24. Comparison of PSD curves for the MBM simulation results and the new regression predictive model against the EHM data for the 1.25 g/cc explosive density design.

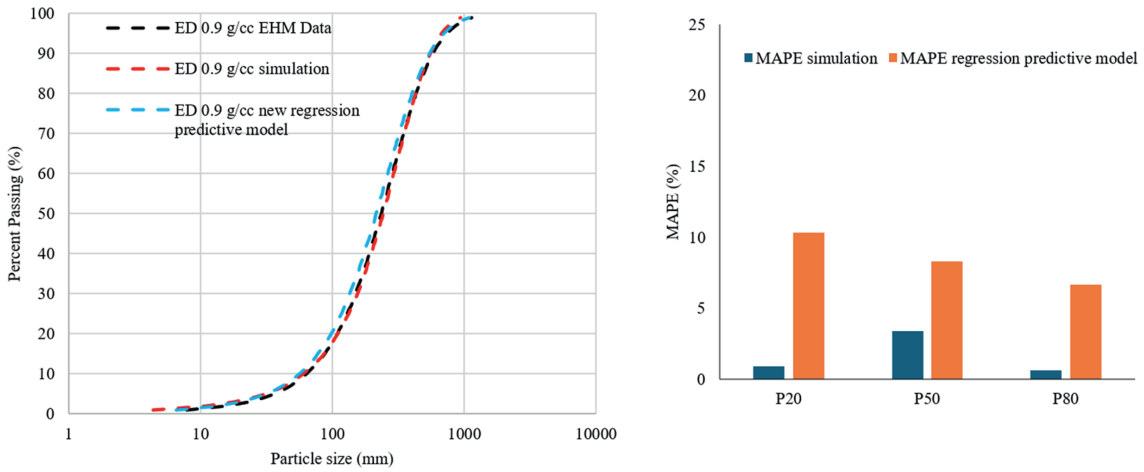

Fig. 25. Comparison of PSD curves for the MBM simulation results and the new regression model against the EHM measured data for the 0.9 g/cc explosive density design.

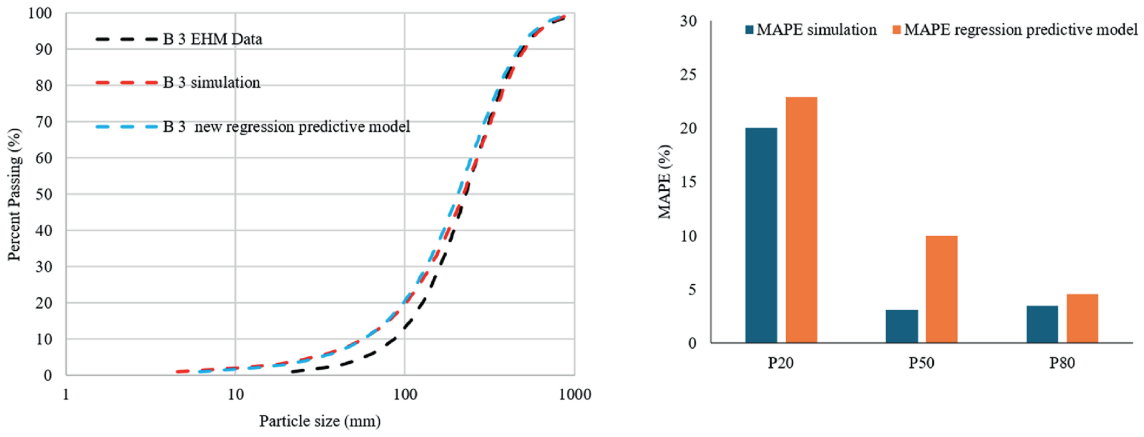

Fig. 26. Comparison of PSD curves for the MBM simulation results and the new regression predictive model against the EHM measured data for the 3.0 m burden design.

passing size data for the new regression model and the numerical simulations are presented in Table 10.

Figs. 27 and 28 compare the PSD data from the new regression model and the MBM simulation for the two different blast designs. Overall, the empirical models produce PSD data that is very close the MBM data, in particularly for the P20 passing size. At P80 and P50 the regression predictive models slightly under predict compared to MBM.

The MAPE for P20, P50, and P80 confirm the very good agreement in PSD curves predicted by the two models (Fig. 29). The absolute differences in P20, P50, and P80 are 2.8%, 5.5%, and 4.8% for NB1, and 1.7%, 2.9%, and 4.7% for NB2, respectively.

Table 10
Fragmentation data from the new empirical model and the numerical simulations.

Size distribution	NB1		NB2	
	New regression models	MBM result	New regression models	MBM result
P20 (mm)	106	109	122	120
P50 (mm)	241	255	266	274
P80 (mm)	435	457	465	488

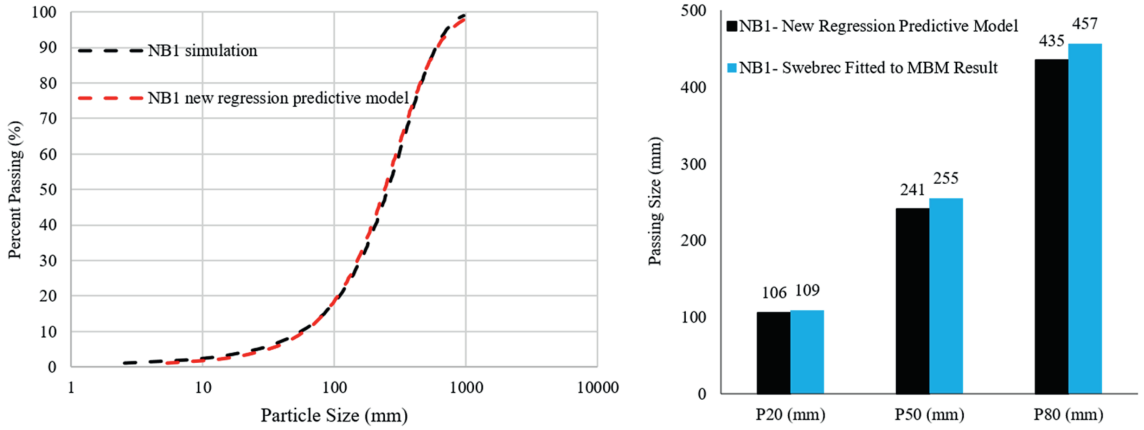

Fig. 27. Comparison of PSD data created by the new regression model and MBM for NB1.

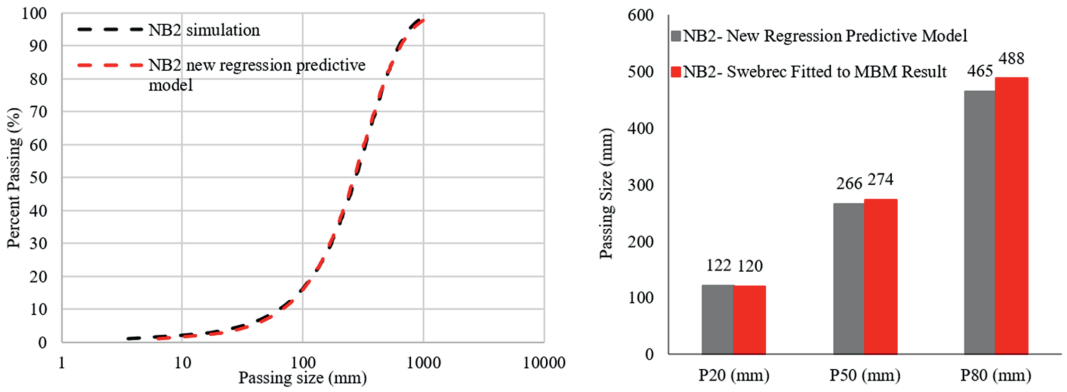

Fig. 28. Comparison of PSD data created by the new regression model and MBM for NB2.

The MBM results provide better predictions of PSD than the new regression predictive model, as shown in Figs. 23–26. However, the new regression model, offers the advantage of efficiency with reasonable accuracy.

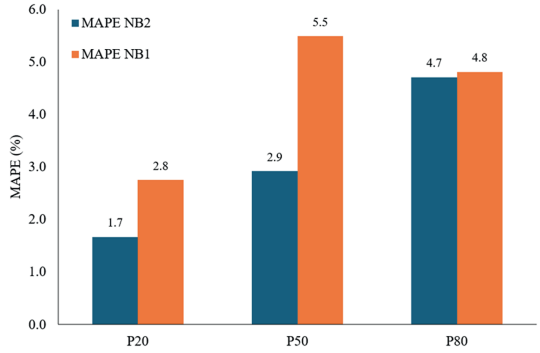

Fig. 29. The MAPE of predictions using the new regression model compared to the MBM results.

5. Conclusions

Fragmentation data from the EHM mine was used to build and calibrate numerical fragmentation models, and to develop and validate new empirical models to help reduce computational requirements in modelling blast-induced fragmentations for SLC operations. A total of 34 different simulations were run in MBM, and their fragmentation data were compared with the EHM measured data. The findings indicate that the numerical simulations could satisfactorily predict rock fragmentation sizes for coarse fractions greater than P65 but were less accurate for smaller size fractions. To address the accuracy issue for smaller fragment sizes, the Swebrec curve was fitted to the simulation results, which was then used to determine P20, P50, and P80 for subsequent multivariate regression analyses. This led to the development of three regression models to predict passing sizes corresponding to P20, P50, and P80.

The modelling input parameters were categorised into four groups. The first is the BDF, including parameters that are related to blast design and can be adjusted by operators, such as burden,

charge spacing, explosive density, and hole diameter. Multiple simulations were run to determine the influences of each blast design parameter on the resulting fragmentation, leading to the establishment of the expression for BDF. The second group is the Rock Property Factor (RPF), incorporating the tensile strength and fracture density parameters. The impact of RPF on P80 passing sizes varied from that on P20 and P50, as fracture frequency played a more significant role in the finer portion of the fragmentation size distribution. The third category is In-Situ Stress (IS), to assess the impact of local stress states on the fragmentation. The final group is the Non-Ideal Detonation Factor, to incorporate the influences of different detonation characteristics on the fragmentation. Note that, in this study, only one type of explosive was used, therefore, the effect of non-ideal detonation parameters has not been examined in the regression analyses.

The developed predictive models have demonstrated strong performance, with R^2 values of 0.87 for P20, 0.85 for P50, and 0.79 for P80. Sensitivity analysis showed that the most influential parameters for fragmentation size distributions are rock property factors, BDF and in-situ stresses, in the order of significance. A major contribution of the new regression models is their ability to incorporate a wide range of variables to estimate fragmentation size distributions in a wide range of different blasting conditions. The developed regression models fit well against the EHM data. To further assess their performances, two additional cases were simulated using MBM. The results again demonstrated that the new models could provide very good predictions for P20, P50, and P80 passing sizes, offering the advantage of avoiding time-consuming numerical simulations.

It is important to note that the developed regression models (the coefficients in these models) are specific to the EHM site due to the site-specific input parameters used in the training simulations. However, the investigation framework and relationships are expected to be at least qualitatively applicable to different SLC operations, providing guidance for fragmentation size-related optimization problems in other mining operations.

CRediT authorship contribution statement

Ahmadreza Khodayari: Writing – review & editing, Writing – original draft, Visualization, Validation, Software, Resources, Methodology, Investigation, Formal analysis, Data curation, Conceptualization. **Chaoshui Xu:** Writing – review & editing, Supervision, Resources, Methodology, Investigation, Formal analysis, Conceptualization. **Peter Dare-Bryan:** Writing – review & editing, Visualization, Software, Resources, Methodology, Investigation, Formal analysis, Conceptualization. **Peter Dowd:** Writing – review & editing, Validation, Supervision, Investigation, Conceptualization. **Veljko Lapcevic:** Writing – review & editing, Validation, Methodology, Formal analysis, Conceptualization. **Andrew Metcalfe:** Writing – review & editing, Validation, Formal analysis, Conceptualization.

Declaration of competing interest

The authors declare that they have no known competing financial interests or personal relationships that could have appeared to influence the work reported in this paper.

Acknowledgements

This research was funded by the Australian Research Council Integrated Operations for Complex Resources Industrial Transformation Training Centre (Grant No. IC190100017) and jointly supported by universities, industry and the Australian Government.

References

Aler, J., Du Mouza, J., Arnould, M., 1996. Measurement of the fragmentation efficiency of rock mass blasting and its mining applications. Int. J. Rock Mech. Min. Sci. Geomech. Abstr. 33 (2), 125–139.

Campbell, A., 2019. Full-Scale Experiments and Numerical Modelling to Improve Ore Recovery in Sublevel Cave Mines. The University of Queensland, Brisbane, Australia. PhD Thesis.

Campbell, A., Power, G., 2017. Improving calibration of flow models against SLC marker trials by linking blasting effects to particle mobility. In: 13th Ausimm Underground Operators' Conference. Gold Coast, Australia.

Campbell, A., Thurley, M., 2017. Application of laser scanning to measure fragmentation in underground mines. Min. Technol. 126 (4), 240–247.

Chitombo, G., Onederra, I., Cundall, P., Furtney, J., Torres, M., Markham, J., 2010. The Hybrid Stress Blasting Model: a Methodology and Numerical Model for Blast Design and Optimisation - Final Report, 2010.

Chung, S.H., Katsabanis, P., 2000. Fragmentation prediction using improved engineering formulae. Fragblast 4 (3–4), 198–207.

Cunningham, C., 1983. The Kuz–Ram model for prediction of fragmentation from blasting. In: Holmberg, R., Rustan, A. (Eds.), Proc. 1st Int. Symp. on Rock Fragmentation by Blasting, Luleå, Sweden. Luleå Tekniska Universitet, Luleå, pp. 22–26 Aug.

Cunningham, C., 1987. Fragmentation estimations and the Kuz–Ram model - four years on. In: Fourney, W.L., Dick, R.D. (Eds.), Proc. 2nd Int. Symp. on Rock Fragmentation by Blasting, Keystone, CO, USA, 23-26 Aug. Society of Experimental Mechanics. Bethel.

Cunningham, C., 2005. The Kuz–Ram fragmentation model - 20 years on. In: Brighton Conference Proceedings. European Federation of Explosives Engineers, Brighton, UK.

Dare-Bryan, P., Mansfield, S., Schoeman, J., 2013. Blast optimisation through computer modelling of fragmentation, heave and damage. In: Rock Fragmentation by Blasting: 10Th Int. Symp. on Rock Fragmentation by Blasting (Fragblast 10). Taylor and Francis Books Ltd., London, UK.

Ding, X., Zhou, W., Lu, X., Li, M., Manda, E., Shi, X., Luan, B., Qi, C., 2019. Distribution characteristics of fragment size and optimisation of blasting parameters under blasting impact load in open-pit mine. IEEE Access 7, 137501–137516.

Djordjevic, N., 1998. Optimal blast fragmentation. Min. Mag. 178 (2), 121.

Djordjevic, N., 1999. A two-component model of blast fragmentation. AusIMM Proc. 2, 9–13.

Esen, S., Onederra, I., Bilgin, H.A., 2003. Modelling the size of the crushed zone around a blasthole. Int. J. Rock Mech. Min. Sci. 40 (4), 485–495.

Furtney, J., Cundall, P., Chitombo, G., 2009. Developments in numerical modelling of blast-induced rock fragmentation: updates from the HSBM project. In: Proc. 9th Int. Symp. on Rock Fragmentation by Blasting (FRAGBLAST 9). CRC Press, Boca Raton, FL, USA.

Grant, J., Little, T., Bettess, D., 1995. Blast-driven mine optimisation. In: Explosives in Mining Conference. Brisbane, Australia, Sept.

Greenland, S., Senn, S.J., Rothman, K.J., Carlin, J.B., Poole, C., Goodman, S.N., Altman, D.G., 2016. Statistical tests, P values, confidence intervals, and power: a guide to misinterpretations. Eur. J. Epidemiol. 31 (4), 337–350.

Hamdi, E., Du Mouza, J., Fleurisson, J., 2001. Evaluation of the part of blasting energy used for rock mass fragmentation. Fragblast 5 (3), 180–193.

Hjelmberg, H., 1983. Some ideas on how to improve calculations of the fragment size distribution in bench blasting. In: Proc. 1st Int. Symp. on Rock Fragmentation by Blasting. Luleå University of Technology, Luleå, Sweden.

Jimeno, C.L., Jimeno, E.L., Carcedo, F.J.A., de Ramiro, Y.V., 1995. Drilling and blasting of rocks. CRC Press, USA, 41, 35947.

Jing, L., 2003. A review of techniques, advances and outstanding issues in numerical modelling for rock mechanics and rock engineering. Int. J. Rock Mech. Min. Sci. 40 (3), 283–353.

Khodayari, A., Xu, C., Dowd, P., Dare-Bryan, P., Metcalfe, A., 2024. Sub-level Caving blast modelling to determine the impact of blast design parameters and rock mass characteristics on fragmentation. In: ARMA US Rock Mechanics/Geomechanics Symposium. ARMA, USA.

Kirby, I., Chan, J., Minchinton, A., 2014. Advances in predicting the effects of non-ideal detonation on blasting. In: Proc. 40th Annual Conference on Explosives and Blasting Techniques. International Society of Explosives Engineers, Denver, CO, USA.

Koshelev, E., Kuznetsov, V., Sofronov, S., Chernikov, A., 1971. Statistics of the fragments forming with the destruction of solids by explosion. J. Appl. Mech. Tech. Phys. 12 (2), 244–256.

Lapčević, V., Torbica, S., Stojanović, M., Vojinović, I., 2023. Development and validation of universal 3D blast fragmentation model. Appl. Sci. 13 (14), 8316.

Lith, A., Kuchta, M., Quinteiro, C., 2004. Prediction of fragmentation for ring blasting in large-scale sublevel caving. In: Proc. 13th Int. Symp. on Mine Planning and Equipment Selection (MPES 2004). Wroclaw, Poland, Sept. CRC Press/Balkema, Leiden, Netherlands.

Manzoor, S., 2023. Role of Fragmentation at the Production Level of a Sublevel Caving Operation. Luleå University of Technology, Luleå, Sweden. PhD Thesis.
Manzoor, S., Gustafson, A., Schunnesson, H., Tariq, M., Wettainen, T., 2022. Rock fragmentation measurements in sublevel caving: field tests at LKAB's Malmberget mine. In: Caving 2022: Proc. 5th Int. Conf. on Block and Sublevel Caving. Australian Centre for Geomechanics, Adelaide, Australia.
Minchinton, A., Dare-Bryan, P., 2005. The application of computer modelling for blasting and flow in sublevel caving operations. In: Proc. 9th AusIMM Underground Operators' Conference. Perth, Australia.
Minchinton, A., Lynch, P.M., 1997. Fragmentation and heave modelling using a coupled discrete element gas flow code. Fragblast 1 (1), 41–57.
Mitchell, T., Wang, Z., Araos, M., Leonardi, C., Gefken, P., Onederra, I., 2023. Experimental and numerical investigation into the fracture patterns induced by blast-loading under unconfined and confined conditions. Rock Mech. Rock Eng. 56 (4), 2433–2455.
Noy, M., 2013. Automated rock fragmentation measurement with close range digital photogrammetry. In: Measurement and Analysis of Blast Fragmentation Workshop (FRAGBLAST).
Onederra, I., 2004a. A fragmentation modelling framework for underground ring blasting applications. Fragblast 8 (3), 177–200.
Onederra, I., 2004b. Breakage and fragmentation modelling for underground production blasting applications. In: IRR Drilling and Blasting Conference 2004. Perth, Australia.
Onederra, I., Esen, S., Jankovic, A., 2004. Estimation of fines generated by blasting - applications for the mining and quarrying industries. Min. Technol. 113 (4), 237–247.
Oñederra, I.A., 2005. A Fragmentation Model for Underground Production Blasting. PhD Thesis. University of Queensland, Brisbane, Australia.
Onederra, I.A., Furtney, J.K., Sellers, E., Iverson, S., 2013. Modelling blast-induced damage from a fully coupled explosive charge. Int. J. Rock Mech. Min. Sci. 58, 73–84.
Ouchterlony, F., 2005. The Swebrec© function: linking fragmentation by blasting and crushing. Min. Tech 114 (1), 29–44.
Ouchterlony, F., Sanchidrián, J.A., 2018. A review of the development of better prediction equations for blast fragmentation. Rock Dynam. Appl. 3, 25–45.
Ouchterlony, F., Sanchidrián, J.A., Moser, P., 2017. Percentile fragment size predictions for blasted rock and the fragmentation-energy fan. Rock Mech. Rock Eng. 50, 751–779.
Owen, D., Munjiza, A., Bicanic, N., 1992. A finite element-discrete element approach to the simulation of rock blasting problems. In: Proc. 11th Symp. on Finite Element Methods.
Ruest, M., Cundall, P., Guest, A., Chitombo, G., 2006. Developments using the particle flow code to simulate rock fragmentation by condensed phase explosives. Fragblast 8, 140–151.
Sanchidrián, J., Segarra, P., Ouchterlony, F., López, L., 2009. On the accuracy of fragment size measurement by image analysis in combination with some distribution functions. Rock Mech. Rock Eng. 42, 95–116.
Sanchidrián, J.A., Ouchterlony, F., 2017. A distribution-free description of fragmentation by blasting based on dimensional analysis. Rock Mech. Rock Eng. 50, 781–806.
Sanchidrián, J.A., Ouchterlony, F., Segarra, P., Moser, P., 2014. Size distribution functions for rock fragments. Int. J. Rock Mech. Min. Sci. 71, 381–394.
Sellers, E., Furtney, J., Onederra, I., Chitombo, G., 2012. Improved understanding of explosive–rock interactions using the hybrid stress blasting model. J. S. Afr. Inst. Min. Metall 112 (8), 721–728.
Shahrin, M.I., Abdullah, R.A., Jeon, S., Jeon, B., Sa'ari, R., 2019. Numerical simulation of rock fragmentation by blasting using discrete element method and particle blast method. In: IOP Conf. Ser.: Mater. Sci. Eng. IOP Publishing.
Shekhar, G., 2020. Draw Control Strategy for Sublevel Caving Mines: a Holistic Approach. Luleå University of Technology, Luleå, Sweden. PhD Thesis.
Stagg, M.S., Rholl, S.A., Otterness, R.E., Smith, N.S., 1990. Influence of shot-design parameters on fragmentation. In: Proc. 3rd Int. Symp. on Rock Fragmentation by Blasting. The Australasian Institute of Mining and Metallurgy, Brisbane, Australia, pp. 311–317.
Thurley, M., Wimmer, M., Nordqvist, A., 2015. Blast fragmentation measurement based on 3D imaging in sublevel caving drawpoints and LHD buckets at LKAB Kiruna. In: Proc. 11th Int. Symp. on Rock Fragmentation by Blasting (FRAGBLAST 11), pp. 763–774. Sydney, Australia, Aug.
Thurley, M.J., 2013. Automated image segmentation and analysis of rock piles in an open-pit mine. In: Proc. 2013 Int. Conf. on Digital Image Computing: Techniques and Applications (DICTA). IEEE, USA.
Weibull, W., 1951. A statistical distribution function of wide applicability. J. Appl. Mech. 18 (3), 293–297.
Wimmer, M., 2012. Towards Understanding Breakage and Flow in Sublevel Caving (SLC): Development of New Measurement Techniques and Results from full-scale Tests. Luleå University of Technology, Luleå, Sweden. PhD Thesis.
Wimmer, M., Ouchterlony, F., 2009. 2D image analysis using WipFrag software compared with actual sieving data of Kiruna magnetite loaded from a drawpoint. Swedish Blast. Res. Centre (Swebrec).
Yang, R., Zhao, Y., Ding, C., Zuo, J., Liu, Y., Ding, L., 2021. Numerical simulations of lowering boulder yield based on delay time and double-primer initiation. Arab. J. Geosci. 14, 1–11.
Yi, C., Johansson, D., Wimmer, M., Nordqvist, A., San Miguel, C., 2022. Numerical modelling of fragmentation by blasting and gravity flow in sublevel caving mines. In: Caving 2022: Proc. 5th Int. Conf. on Block and Sublevel Caving, Australian Centre for Geomechanics. Adelaide, Australia.
Yi, C., Sjöberg, J., Johansson, D., 2017. Numerical modelling for blast-induced fragmentation in sublevel caving mines. Tunn. Undergr. Space Technol. 68, 167–173.
Zhang, Z., Gao, W., Li, K., Li, B., 2020. Numerical simulation of rock mass blasting using particle flow code and particle expansion loading algorithm. Simulat. Model. Pract. Theor. 104, 102119.

Ahmadreza (Reza) Khodayari is a PhD candidate in Mining Engineering at the University of Adelaide (since April 2023), focusing on drawpoint and cave operations and fragmentation sensing. He holds a BSc in Mining Engineering from Imam Khomeini International University (2018) and an MSc from Amirkabir University of Technology (2021). His research interests include sublevel-caving blast modelling, gravity flow and fragmentation analysis, fracture mechanics, 3D numerical simulation, and data-driven methods. His recent publications cover topics such as a machine-learning approach to predicting blast-induced fragment size (FRAGBLAST, 2025), sublevel-caving blast modelling (ARMA, 2024), and the impact of explosive-charge misfires on gravity flow (MassMin, 2024).